Submitted to the 30th International Conference on High-Energy Physics ICHEP2000,
Osaka, Japan, July 2000

A Measurement of Single-Inclusive Jet Cross Sections in the Central and Forward Region at low x in DIS at HERA

H1 Collaboration

Abstract

We present a measurement of single-inclusive jet cross sections as a function of the transverse energy of the jet, E_T, the ratio of the transverse energy squared over the photon virtuality, E_T^2/Q^2, and the Bjorken scaling variable, x_{Bj}, for jets with a transverse energy $E_T > 5$ GeV in the Breit reference frame and a pseudorapidity in the laboratory frame η_{lab} between -1.0 and 2.8. The analysis is performed on data corresponding to an integrated luminosity of about 21 pb^{-1} taken with the H1 detector in 1996/97 in the region $5 < Q^2 < 100\ \mathrm{GeV}^2$ and $10^{-4} \lesssim x_{Bj} \lesssim 5 \cdot 10^{-3}$. The distributions are measured in different ranges of Q^2 and η_{lab}. The data are compared to fixed order QCD calculations using E_T^2 or Q^2 as renormalization scale μ_R^2. None of the two choices is able to describe the data over the full phase space. Especially for $\mu_R^2 = E_T^2$ large discrepancies are observed in the forward direction for low $Q^2 \lesssim 20\ \mathrm{GeV}^2$, low $E_T \lesssim 20$ GeV and low $x_{Bj} \lesssim 10^{-3}$. The observed discrepancies leave room for additional cross section contributions from higher orders, resolved photon processes or modified parton dynamics.

Abstract: 999
Parallel session: 3
Plenary talk: 11

1 Introduction

The HERA machine, colliding electrons or positrons on protons at a center-of-mass energy of about 300 GeV, offers an ideal testing ground for the theory of strong interactions in deep-inelastic scattering (DIS). The large available phase space allows for the production of highly energetic hadrons which emerge from short-distance processes and to probe in a previously unexplored kinematic domain the detailed characteristics of the hadronic final state in which clear jet structures can be observed. These jets - sprays of almost collinear hadrons - form a link between the fundamental objects of the theory of strong interactions - quarks and gluons - and the hadrons observed in the final state.

In the Breit reference frame, where the parton and the photon collide head-on, the transverse energy E_T of jets in the final state is exclusively produced by the underlying hard QCD process and reflects its hardness[1]. E_T therefore is a natural scale in the process. However, also the photon virtuality Q^2 can be a hard scale, as for example in inclusive measurements of the total DIS cross section. It is therefore interesting to study the interplay of these two QCD scales. Aside from E_T also the pseudorapidity η and the Bjorken scaling variable x_{Bj} characterize the short distance scattering process.

Jet cross sections can be calculated using the $\mathcal{O}(\alpha_s^2)$ matrix elements together with parton density functions based on the DGLAP (Dokshitzer-Gribov-Lipatov-Altarelli-Parisi) parton evolution formalism[1]. This formalism works remarkably well for totally inclusive measurements like that of the proton structure function F_2 at HERA[2, 3]. However, the assumptions made to derive the DGLAP equations should loose their validity in the low-x_{Bj} regime at HERA. In addition, in the forward region towards the proton remnant the production of high transverse energy jets should be suppressed according to the DGLAP formalism. Therefore a 'forward jet' regime was suggested by several authors[4, 5, 6] as a possible way to observe the onset of an alternative parton evolution scheme, the BFKL (Balitsky-Fadin-Kuraev-Lipatov) formalism[7]. Recent results on forward jets from the HERA experiments[8, 9] show discrepancies between data and LO QCD Monte Carlo models and $\mathcal{O}(\alpha_S^2)$ QCD calculations. However, it was not studied whether the models and calculations are able to describe the data in a wider, more general phase space.

There are other possible explanations for the discrepancies observed in[8, 9]. First, the calculations might have significant corrections from higher orders in the perturbation series, e.g. $\mathcal{O}(\alpha_S^3)$, which have not yet been calculated. Second, the effects of a resolved hadronic substructure of the virtual photon can play an important role for the cross section if $Q^2 \lesssim E_T^2$, i.e. if a parton emitted from the proton can act as a probe on the photon.

In this analysis we measure jet cross sections in a large phase space ($5 < Q^2 < 100\ \mathrm{GeV}^2$, $10^{-4} \lesssim x_{Bj} \lesssim 5 \cdot 10^{-3}$, $-1.0 < \eta_{lab} < 2.8$, with η_{lab} the pseudorapidity in the laboratory reference frame) as a function of E_T, E_T^2/Q^2 and x_{Bj}. The jet measurements are done single-inclusively, i.e. by counting single jets that pass certain selection criteria. This seems to be the most basic way to test the predictions of perturbative QCD for jet production. After measurements in the wide phase space we use the highly increased amount of available data as compared to[8] to

[1]The Breit frame is defined by $\vec{q} + 2x_{Bj}\vec{P} = 0$, where $\vec{q}$ and $\vec{P}$ are the momenta of the exchanged photon and the incoming proton.

perform a detailed analysis in specific phase space regions. In particular we study the forward jet regime and compare the data to NLO QCD calculations.

This paper is organized as follows: Section 2 gives an overview over the theoretical framework of jet cross sections and parton evolution schemes and introduces the notion of forward jets. Section 3 describes the QCD fixed order calculations and QCD Monte Carlo generators used in this analysis. Section 4 gives an overview of the components of the H1 detector which are particularly important for this analysis. Section 5 describes the data selection, section 6 presents the results.

2 Theoretical Background

For the analytic derivation of jet cross sections matrix elements of the hard scattering and input parton density functions have to be considered. The hard scattering process can be calculated using a perturbative expansion in the strong coupling constant α_S. The Feynman graphs of fig. 1 show different contributions to the hard scattering. Fig. 1a represents an example of a process of leading order (LO) or $\mathcal{O}(\alpha_S)$. In fig. 1b, an additional gluon is radiated, corresponding to $\mathcal{O}(\alpha_S^2)$ or next-to-leading order (NLO). Even more partons can be emitted from either the original parton emitted by the proton or from any other parton of the final state. Such higher orders (NNLO, NNNLO,...) cannot yet be calculated exactly.

The input parton density functions are obtained from fits to a variety of data sets according to the DGLAP evolution formalism[1]. The DGLAP formalism is based on the assumption of strong k_T ordering of the partons emitted along a parton ladder (see fig. 2): $k_{Tn}^2 \gg k_{Tn-1}^2 \gg ... \gg k_{T1}^2$. There is only a soft ordering of the fractional longitudinal parton momenta, $x_n < x_{n-1} < ... < x_1$. The formalism corresponds to a resummation of terms of the form $\alpha_S \cdot \log Q^2$. An alternative evolution scheme is based on the BFKL equation[7] which should be valid at small x_{Bj} and which assumes a strong ordering in the fractional longitudinal parton momenta, $x_n \ll x_{n-1} \ll ... \ll x_1$. The BFKL formalism leads to a random distribution of the transverse momenta k_{Ti}; it corresponds to a resummation of terms of the form $\alpha_S \cdot \log \frac{1}{x}$.

Both evolution equations are complementary approximations to a more complete calculation. In the low-x regime the $\alpha_S \cdot \log \frac{1}{x}$ terms get large and the observation of a deviation from the DGLAP formalism should be possible, in particular in the region as close as possible to the proton remnant. Here the emission of partons with high E_T and therefore also the jet cross sections are suppressed in the DGLAP picture. This 'forward jet region' is particularly suited to observe BFKL effects[4, 5, 6, 8, 9]. In more detail this region is defined by large jet pseudorapidities η_{lab}, large scaled jet energies $x_{Jet} \equiv E_{Jet}/E_p$ (with E_p the proton energy) and a scaled transverse jet energy E_T^2/Q^2 of the order of 1. The first and the third condition suppress DGLAP contributions due to the strong k_T ordering which does not allow high E_T partons close to the proton remnant; for low x_{Bj} the second requirement provides a large phase space for the emission of partons along the ladder.

For sufficiently small Q^2 or $Q^2 \lesssim E_T^2$ the parton emitted by the proton is able to probe the hadronic substructure of the photon. In this case the photon can be considered as a source of partons and additional ('resolved') processes enhancing the cross section can occur, see fig. 1c and 1d for examples of LO and NLO resolved processes. It was argued in [10] that the NLO direct and resolved diagrams can be taken as an approximation of the $\mathcal{O}(\alpha_S^3)$ direct calculation.

3 QCD Calculations and Models

3.1 $\mathcal{O}(\alpha_S^2)$ QCD Calculations

There are currently several computer programs which implement calculations of jet cross sections up to $\mathcal{O}(\alpha_s^2)$ like MEPJET[11], DISENT[12], DISASTER++[13] and JetViP[14]. Comparisons of these programs can be found in [15]. In this analysis we compare our data to the DISENT and JetViP programs.

The DISENT program[12] is based on the subtraction method for the cancelation of divergencies which occur in the calculation of the hard scattering cross section when soft or collinear partons are emitted. The program calculates direct photon processes only, i.e. processes where the photon is regarded as pointlike to the order $\mathcal{O}(\alpha_S^2)$. In this analysis we have set the renormalization scale μ_R^2 either to Q^2 or E_T^2 and the factorization scale μ_F^2 to Q^2. The influence of the factorization scale is usually small for the jet cross sections presented here.

The JetViP program[14] takes, in addition to direct processes, also resolved photon processes into account. The parton density functions of the photon evolved in the DGLAP formalism are used. JetViP is based on the phase-space slicing method for the treatment of infrared and collinear divergencies. This method introduces an unphysical arbitrary parameter y_{cut} to isolate these infrared and collinear divergencies associated with regions where two partons cannot be resolved. Two partons are unresolvable if their invariant mass $s_{ij} \equiv 2 \cdot p_i \cdot p_j$ is smaller than y_{cut}. The renormalization and factorization scales are always set to the same value which was chosen to be $Q^2 + E_T^2$. This choice assures that the hard scattering scale is always larger than the photon virtuality.

The matrix element calculation and the kinematics of resolved photon processes in JetViP are done in the limit of vanishing quark masses and for on-shell partons, i.e. zero virtuality. This is consistent with the construction of the parton density functions which have been derived for on-shell partons. However, for photon virtualities $Q^2 \gg 1\ \mathrm{GeV}^2$ mass and k_T effects in the parton emission from the photon will become important, but they are not included in the original JetViP program[14]. It is therefore not clear whether the JetViP calculations for the resolved processes will work well for larger Q^2. One way to improve the situation for larger Q^2 studied in [10] is to approximately include the mass effects by combining virtual quarks with the massless matrix elements. This, however, leads to a dependence of the cross sections on the unphysical y_{cut} parameter. We will study both versions ('on-shell scheme' and 'off-shell scheme') in the following.

Both the DISENT and the JetViP calculations where performed using the CTEQ4M[16] proton parton density functions. The strong coupling constant is taken to be consistent with the one used in the parton density function, where $\Lambda_{\overline{MS}}^{(5)}$ = 0.202 GeV for five flavours.

3.2 QCD Monte Carlo Models

Simulations of the detailed properties of the hadronic final state are available in the form of Monte Carlo event generators.

The LEPTO 6.5[17] and RAPGAP 2.06[18] Monte Carlos use $\mathcal{O}(\alpha_S)$ matrix elements for the calculation of the hard subprocess and leave the simulation of higher orders to matched parton showers which take into account leading logarithms to all orders. The ARIADNE 4.08[19] Monte Carlo simulates the parton cascade by a chain of independently radiating color dipoles according to the Colour Dipole Model (CDM)[20]. Unlike in LEPTO, the parton emissions in ARIADNE are not ordered in k_T[21]. The $\mathcal{O}(\alpha_S)$ matrix elements for photon-gluon fusion events have to be added to the CDM.

The hadronisation of the partonic system for all Monte Carlo generators was modelled using the Lund colour string model as implemented in JETSET[22].

4 The H1 Detector

A detailed description of the H1 detector can be found elsewhere[23]. The following section briefly describes the components of the detector relevant to this analysis: The SPACAL and LAr calorimeters and the tracking system.

The scattered lepton is measured with the backward optical scintillator calorimeter SPACAL[24]. The SPACAL covers the polar range $153° < \theta < 177.8°$. It provides an electromagnetic energy resolution of $\sigma(E)/E = 7.5\%/\sqrt{E/GeV} \oplus 2\%$ and has in addition a hadronic section resulting in two interaction lengths in total.

The hadronic energy flow is mainly measured with the liquid argon (LAr) calorimeter[25] which extends over the polar range $4° < \theta < 154°$ with full azimuthal coverage. It consists of an electromagnetic section with lead absorbers and a hadronic section with steel absorbers. Both sections are highly segmented in polar and azimuthal angle, having about 45 000 channels in total. Test beam measurements of LAr calorimeter modules have shown an energy resolution of $\sigma(E)/E \approx 0.12/\sqrt{E/GeV} \oplus 0.01$ for electrons[26] and of $\sigma(E)/E \approx 0.50/\sqrt{E/GeV} \oplus 0.02$ for charged pions[27]. The hadronic energy measurement is performed by applying a weighting technique in order to account for the non-compensating nature of the calorimeter. The total depth of the LAr calorimeter varies between 4.5 and 8 interactions lengths in the angular range $4° < \theta < 128°$.

The calorimeters are surrounded by a superconducting solenoid providing a uniform magnetic field of 1.15 T oriented parallel to the beam axis. Charged particles are measured in a central tracking device (CT) which covers the polar range $20° < \theta < 160°$[28]. The CT consists of inner and outer cylindrical jet chambers, z-drift chambers and proportional chambers. The jet chambers are mounted around the beam pipe and provide a maximum of 65 space points in the radial plane for tracks with sufficiently large transverse momentum. A backward drift chamber (BDC) in front of the SPACAL improves the identification of the scattered lepton.

The luminosity is measured from elastic Bethe-Heitler events. The final state positron and photon are detected in calorimeters situated at 33 m and 103 m from the interaction vertex in the positron beam direction.

5 Data Selection

The data presented in this paper have been taken in the years 1996/1997 and correspond to an integrated luminosity of about 21 pb^{-1}. During this run period HERA collided 27.5 GeV positrons on 820 GeV protons.

5.1 DIS Event Selection

The data were triggered by requiring an electromagnetic energy deposition of at least 6 GeV in the backward calorimeter SPACAL, indicating a positron candidate, and some loose track requirements. The scattered positron is defined as the highest energetic electromagnetic shower in the SPACAL within a polar angle of $156° < \theta < 176°$ and with a minimum energy of 10 GeV. The analysis was performed in the phase space $5 < Q^2 < 100\ \mathrm{GeV}^2$ and $0.2 < y < 0.6$. For $Q^2 \gtrsim 60\ \mathrm{GeV}^2$ the cut $\theta > 156°$ further limits the phase space. These requirements lead to a range $10^{-4} \lesssim x_{Bj} \lesssim 5 \cdot 10^{-3}$ in the Bjorken scaling variable x_{Bj}. The kinematic quantities were reconstructed from the polar angle of the positron θ_e (measured with respect to the proton beam direction) and from the energy of the scattered positron E'_e using $Q^2 = 4E_eE'_e\cos^2(\theta_e/2)$, $y = 1 - (E'_e/E_e)\sin^2(\theta_e/2)$ and $x_{Bj} = Q^2/(ys)$, were E_e is the incident positron beam energy and s the square of the center-of-mass energy. In this phase space the energy of the scattered positron E'_e is always larger than 10 GeV.

The hadronic final state is reconstructed from low momentum tracks and energy depositions in the SPACAL and LAr calorimeters. Double counting of energy depositions between clusters and tracks is avoided by neglecting the energy measured in the electromagnetic (hadronic) calorimeter in a cylinder with radius 25 (50) cm around the axis given by the direction of a low momentum track. However, if the total energy in such a cylinder is larger than the track energy, only calorimeter information is considered[2]. Using this method energy losses in the calorimeter due to dead material and noise suppression are compensated.

Further suppression of misidentified photoproduction events, initial state QED radiation background and badly measured events was achieved by a cut on the quantity $\Sigma_i(E_i - p_{z,i})$ where the sum runs over all final state objects. This quantity had to be between 45 and 65 GeV. The events were required to have an event vertex within 35 cm of the nominal vertex position.

The selected inclusive DIS data sample consists of approximately 820.000 events. The photoproduction background in this sample was estimated to be smaller than 3 $\%$ and was neglected in the following analysis.

5.2 Jet Selection and Definition of Observables

Jets are defined with the inclusive k_T cluster algorithm[29] which is applied to all objects of the hadronic final state discussed above, to stable hadrons or to partons. The scattered lepton is excluded from the jet finding. For a complete description and an exact definition of how this algorithm has been used in this analysis see [30]. The jet finding was performed in the Breit reference frame.

The jets were selected by demanding a minimum transverse energy E_T of 5 GeV in the Breit frame and a pseudorapidity in the laboratory frame well within the LAr calorimeter acceptance, -1.0 < η_{lab} < 2.8. The lower limit corresponds to the backward direction; the upper limit marks the very forward detector region towards the proton remnant and corresponds to approximately 7 degree. There are 104.000 events with at least one such jet; 34.000 events have two such jets, 4.600 have three and 530 events have even four such jets.

Each jet which fulfills the above requirements enters in the measurements of single-inclusive jet cross sections. The following single-inclusive jet cross sections are measured:

- the cross section $d\sigma_{Jet}/dE_T$ as a function of the transverse energy E_T in different ranges of the pseudorapidity η_{lab} and of the photon virtuality Q^2,
- the cross section $d\sigma_{Jet}/d(E_T^2/Q^2)$ as a function of the ratio E_T^2/Q^2, also in ranges of η_{lab} and Q^2, and finally
- the cross section $d\sigma_{Jet}/dx_{Bj}$ as a function of x_{Bj} for two rapidity regions. An additional cut on the fractional jet energy $x_{Jet} \equiv E_{Jet}/E_p$ (with E_p the proton beam energy and both E_{Jet} and E_p measured in the laboratory frame) is imposed on these distributions. However, in contrast to a former H1 analysis[8] no cut on the ratio E_T^2/Q^2 is performed. This brings the analysis closer to a recent analysis of forward π^0 production[32].

5.3 Correction Procedure and Systematic Errors

The QCD Monte Carlo models RAPGAP and ARIADNE are well able to describe distributions of the kinematic variables Q^2, x_{Bj} or y in the inclusive DIS data sample. Also variables like the ratio of the measured positron energy and the positron energy reconstructed from the double angle method[31] and quantities describing the hadronic final state like the balance between hadronic and positron transverse energy in the event can be well reproduced, showing an overall good understanding of the calibration of the calorimeter.

All data cross sections shown in this paper have been corrected bin-by-bin for detector and QED radiation effects using the ARIADNE and RAPGAP event generators and the simulation of the H1 detector. HERACLES[33] was used to correct for QED radiation. The migration between the bins due to the limited detector resolution was found to be small. The quality of the description of jet cross sections by the two models depends on the transverse energy E_T. The ARIADNE model describes the data at low values of the transverse energy whereas it is too high at E_T values larger than 20 GeV. The RAPGAP model undershoots the data significantly at low E_T, but it agrees quite well with the data at high $E_T \gtrsim$ 20 GeV. Although the jet cross section estimates of the two models differ considerably, the factors used to correct for detector effects derived from the two models agree well and deviate from unity by usually less than 20 $\%$. The difference between the correction factors from the two models is taken as an estimate of the systematic uncertainty of the correction procedure. We also investigated jet profiles in order to check the simulation of the hadronic energy flow in the events (see also [30]) and found them to be well described by the Monte Carlo models.

The hadronisation corrections were estimated using the LEPTO and ARIADNE Monte Carlos. The mean of the two predictions was taken to be the correction factor which was later applied to the parton-level QCD calculations; the difference served as an estimate for the uncertainty of our knowledge of the hadronisation corrections.

We tested another method to reconstruct the event kinematics which involves in addition to the positron also the hadronic final state. The results where compatible; the differences were treated as a systematic uncertainty. Further systematic uncertainties were determined by varying the energy depositions in the LAr (SPACAL) calorimeters by ± 4 % (± 7 %). In addition, the track momenta entering in the definition of the hadronic final state were changed by ± 3 %. The uncertainty on the energy measurement of the scattered positron is taken to be ± 1 %. Additional uncertainties come from the resolution of the angle of the scattered positron (± 2 mrd) and from the total luminosity normalization (± 1.5 %). All errors are added in quadrature and are included in all the following results. The total systematic error is typically of the order of 15 %, the main contribution coming from the uncertainty of the hadronic energy scale.

6 Results

All following cross sections are measured for the kinematic range $5 < Q^2 < 100\ \mathrm{GeV}^2$, $0.2 < y < 0.6$; the transverse energy E_T is always measured in the Breit reference frame. The inner error bars always indicate the statistical errors only, the total error bars include also the systematic errors added in quadrature. All NLO calculations are based on DISENT if not stated otherwise.

The measured jet cross section $d\sigma_{Jet}/dE_T$ as a function of the transverse jet energy E_T in three regions of the pseudorapidity for the total Q^2 range from 5 to 100 GeV^2 is shown in fig. 3. The cross section falls over four orders of magnitude. E_T values up to 60 GeV are reached. In the top part, the cross section is compared to NLO QCD calculations using E_T^2 as renormalization scale (dotted line). Also shown is the uncertainty of the NLO prediction (shaded band) which is estimated by varying the renormalization scale μ_R^2 a factor of four up and down, henceforth referred to as renormalization scale uncertainty. The LO prediction is shown as a dashed line. The hadronisation corrections and their uncertainties are indicated in the center of the figure, they are typically of the order of 10-15 %. The hadronisation corrections lower the QCD predictions. In the bottom part of the figure the ratio $(NLO - Data)/Data$ is displayed, where NLO now is the QCD prediction including hadronisation corrections. The inner, darker shaded band reflects the uncertainty of the hadronisation correction, the total shaded area also includes the uncertainty from the variation of the renormalization scale μ_R^2. It can be observed that at high $E_T \gtrsim$ 20 GeV the data are well described by the NLO QCD calculations in all regions of η_{lab}, whereas at low E_T the QCD prediction is up to a factor of 2 below the data for the forward and slightly below the data in the central rapidity region. The NLO predictions generally describe the data much better than the LO calculations. In regions with discrepancies between data and the theoretical predictions the estimated renormalization scale uncertainties, the difference between the LO and the NLO predictions and the hadronisation corrections are found to be large.

Fig. 4 shows the same data, but now $\mu_R^2 = Q^2$ is chosen as renormalization scale. Now for $E_T \lesssim$ 20 GeV the data are described by the calculation for all values of η_{lab}. However, there is a slight tendency of the calculations to overshoot the data at high values of the transverse energy,

$E_T \gtrsim$ 20 GeV. The obtained renormalization scale uncertainties are much larger for this choice of scale than for $\mu_R^2 = E_T^2$, especially for high values of E_T where they are up to twice as large.

Figs. 5 and 6 present the ratio $(NLO - Data)/Data$ for the cross section $d\sigma_{Jet}/dE_T$ as a function of E_T in the two ranges $5 < Q^2 < 20\ \mathrm{GeV}^2$ and $20 < Q^2 < 100\ \mathrm{GeV}^2$ for $\mu_R^2 = E_T^2$ and $\mu_R^2 = Q^2$, respectively. Again, the dark shaded band reflects the hadronisation uncertainty; the total shaded area includes also the uncertainty from the variation of the renormalization scale. For $\mu_R^2 = E_T^2$, the discrepancies between data and the NLO calculation for low E_T in the forward direction get significant for the lower Q^2 region. For $\mu_R^2 = Q^2$, the excess of the NLO calculation over the data for 20 $\lesssim E_T \lesssim$ 40 GeV is also more pronounced for the lower Q^2 range.

Fig. 7 shows the cross section $d\sigma_{Jet}/dE_T$ as a function of E_T for the forward direction $1.5 < \eta_{lab} < 2.8$ in 5 different ranges of the photon virtuality Q^2. The data are compared to NLO QCD predictions using E_T^2 as renormalization scale. Only for low $E_T \lesssim$ 20 GeV and $Q^2 \lesssim 40\ \mathrm{GeV}^2$ there is a discrepancy between data and the predictions. The picture changes again when we consider the renormalization scale Q^2 (see fig. 8). In this case the description of the data by the calculation is satisfactory everywhere when all errors and uncertainties are taken into account, except for the range in transverse energy from 20 to 40 GeV where the calculations overshoot the data for low $Q^2 < 40\ \mathrm{GeV}^2$. The estimated scale uncertainties are again up to almost twice as large as for a choice $\mu_R^2 = E_T^2$.

Similar conclusions can be drawn from the cross section $d\sigma_{Jet}/(dE_T^2/Q^2)$ as a function of E_T^2/Q^2 in different ranges of the pseudorapidity for the complete range of Q^2 (fig. 9). In the top part, the data are compared to a NLO calculation of the cross section using $\mu_R^2 = E_T^2$. Good agreement between data and calculations for the backward part of the detector is observed, but for the central and forward direction for values of the ratio E_T^2/Q^2 between 2 and 50 discrepancies are revealed. In the central and forward region also the corrections between LO and NLO predictions get very large up to a factor 5. However, for a choice $\mu_R^2 = Q^2$, fig. 10, the data are quite well described by the NLO calculation, except for the largest values of $E_T^2/Q^2 > 50$ where the calculation overshoots the data slightly. This may reflect the discrepancies observed in the cross section $d\sigma_{Jet}/dE_T$ for high values of E_T (compare fig. 4).

Fig. 11 and 12 show, for the cross section $d\sigma_{Jet}/(dE_T^2/Q^2)$ as a function of E_T^2/Q^2, the ratio $(NLO - Data)/Data$ in the two ranges $5 < Q^2 < 20\ \mathrm{GeV}^2$ and $20 < Q^2 < 100\ \mathrm{GeV}^2$ for renormalization scales E_T^2 and Q^2, respectively. Especially for $\mu_R^2 = E_T^2$ the discrepancies between data and NLO QCD calculations are more pronounced in the lower Q^2 range. As for the E_T distributions the estimated scale uncertainties are much larger for $\mu_R^2 = Q^2$.

Fig. 13 illustrates the cross section $d\sigma_{Jet}/dx_{Bj}$ as a function of x_{Bj} in two different regions of η_{lab} for the total range $5 < Q^2 < 100\ \mathrm{GeV}^2$. For these distributions an additional cut $x_{Jet} \equiv E_{Jet}/E_p > 0.035$ was applied to the data. The NLO calculations are based on the renormalization scale E_T^2. In the central rapidity region (left column) the data are described by the calculation within the errors. But in the forward region (right column) for low values of $x_{Bj} \lesssim 10^{-3}$ the data are up to twice as high as the theoretical predictions, with differences increasing as x_{Bj} decreases. This effect was also observed in an H1 analysis of forward π^0 production[32]. As for the distributions of $d\sigma/dE_T$, the situation changes when we assume Q^2 to be the right scale, see fig. 14. Here the data are described by the calculations for all values of the Bjorken scaling variable within the errors and uncertainties. The differences are largest for low values of x_{Bj} in the central rapidity region. However, the obtained renormalization scale uncertainties are up to three times as large as for $\mu_R^2 = E_T^2$.

Fig. 15 summarizes the results for the ratio $(NLO - Data)/Data$ for the x_{Bj} distributions for $\mu_R^2 = E_T^2$ and for $\mu_R^2 = Q^2$ and two regions of the pseudorapidity. The different sizes of the renormalization scale uncertainties are clearly visible.

We also compared our data to the cross section predictions of the JetViP program for direct and resolved photon processes. Fig. 16 shows the cross section $d\sigma_{Jet}/d(E_T^2/Q^2)$ as a function of E_T^2/Q^2 in three different regions of the pseudorapidity. The data points are compared to three different JetViP predictions, one according to the on-shell scheme and two according to the off-shell scheme for two different values of the parameter y_{cut}, see section 3. It can be seen that the three JetViP predictions differ considerably, as may be expected from the discussion in section 3. We also note that none of the different choices is able to describe the data over the whole phase space. Therefore, a physical interpretation of the observed discrepancies between direct NLO calculations and the data as a sign for the need of resolved photon processes in DIS has to wait for a better understanding of the ambiguities in NLO calculations of resolved processes for $Q^2 \gtrsim 5$ GeV^2. A recently published comparison of ZEUS data on E_T^2/Q^2 distributions of forward jets and JetViP calculations of direct and resolved photon processes[34] obtained good agreement in a particular phase space region and a specific choice in the calculations.

Summarizing the jet cross section measurements we can state that using Q^2 as renormalization scale the data are not well described at high values of E_T or E_T^2/Q^2. Since in these regions the calculations tend to be too high, it may be concluded that in these parts of the phase space Q^2 is too low to be the dominant hard scale. In addition, there are very large scale uncertainties observed for this choice of scale. If, however, E_T is chosen as scale, there are various possible interpretations of the observed discrepancies at low Q^2 and low E_T:

First, the calculations might be lacking higher orders in the perturbative series. When implemented, these could increase the cross section predictions in the according to the DGLAP formalism kinematically suppressed forward direction. Cross section calculations of the order $\mathcal{O}(\alpha_S^3)$ are, however, not yet available. Second, the parton evolution in the low Q^2, low x_{Bj} region might require to take BFKL-type dynamics into account. However, up to now there is no BFKL QCD calculation available for our data. Third, in this analysis it could not be clarified whether resolved photon contributions to the cross section would be sufficient to remove the disagreement between data and direct NLO calculations. This is because the only available NLO QCD calculation of such processes, implemented in JetViP, gives no consistent description of the data over the full phase space (in the 'on-shell' scheme) or depends on the unphysical resolution parameter y_{cut} which limits the predictive power of this model (in the 'off-shell' scheme).

7 Conclusions

We have measured single-inclusive jet cross sections in the low Q^2 regime ($5 < Q^2 < 100\,\mathrm{GeV}^2$) in DIS as a function of E_T, E_T^2/Q^2 and x_{Bj} in different regions of the pseudorapidity and of the photon virtuality. A comparison of the data to NLO QCD calculations showed in general good agreement for the backward and central detector regions. However, when going to the forward direction, i.e. to large pseudorapidities, discrepancies between data and NLO calculations are observed. The choice $\mu_R^2 = E_T^2$ for the renormalization scale leads to discrepancies of up to a factor 2 at low values of the transverse energy $E_T \lesssim$ 20 GeV, for values of the ratio E_T^2/Q^2 between 2 and 50 and for low values of the Bjorken scaling variable $x_{Bj} \lesssim 10^{-3}$. The discrepancies are usually largest in regions where also the difference between leading and next-to-leading order QCD predictions, the hadronisation corrections and the renormalization scale uncertainties are large. They are prominent for low values of $Q^2 < 20\ \mathrm{GeV}^2$. Choosing however $\mu_R^2 = Q^2$ the data are in overall good agreement with the theoretical predictions. Only for high values of E_T between 20 and 40 GeV and for $E_T^2/Q^2 > 50$ the QCD calculations overshoot the data. However, for $\mu_R^2 = Q^2$ the obtained renormalization scale dependencies are larger than for $\mu_R^2 = E_T^2$ by up to a factor of 3.

A more satisfactory interpretation of the present results might be possible when higher order calculations based on the DGLAP equations, BFKL-type calculations and also a consistent treatment of resolved photon processes in the kinematic range of our data will be available.

Acknowledgements

We are grateful to the HERA machine group whose outstanding efforts have made and continue to make this experiment possible. We thank the engineers and technicians for their work in constructing and now maintaining the H1 detector, our funding agencies for financial support, the DESY technical staff for continual assistance, and the DESY directorate for the hospitality which they extend to the non DESY members of the collaboration. We also would like to thank M.H. Seymour and B. Pötter for invaluable discussions and help with their QCD programs.

References

[1] V.N. Gribov and L.N. Lipatov, *Sov. J. Nucl. Phys.* **15** (1972) 438,675;
Yu.L. Dokshitzer, *Sov. Phys. JETP* **46** (1977) 641;
G. Altarelli and G. Parisi, *Nucl. Phys.* **B 126** (1977) 297.

[2] H1 Collab., C. Adloff et al., *Eur. Phys. J.* **C 13** (2000) 609.

[3] ZEUS Collab., J. Breitweg et al., *Eur. Phys. J.* **C 11** (1999) 427.

[4] A.H. Mueller, *Nucl. Phys. B (Proc. Suppl.)* **18C** (1990) 125; *J. Phys.* **G 17** (1991) 1443.

[5] J. Kwieciński, A.D. Martin and P.J. Sutton, *Phys. Rev.* **D 46** (1992) 921.

[6] J. Bartels, A. De Roeck and M. Loewe, *Z. Phys.* **C 54** (1992) 635;
W.K. Tung, *Phys. Lett.* **B 278** (1992) 363.

[7] E.A. Kuraev, L.N. Lipatov and V.S. Fadin, *Sov. Phys. JETP* **45** (1972) 199;
Y.Y. Balitski and L.N. Lipatov, *Sov. J. Nucl. Phys.* **28** (1978) 822.

[8] H1 Collab., C.Adloff et al., *Nucl. Phys.* **B 538** (1999) 3.

[9] ZEUS Collab., J. Breitweg et al., *Eur. Phys. J.* **C 6** (1999) 239.

[10] G. Kramer and B. Pötter, *Phys. Lett.* **B 453** (1999) 295.

[11] E. Mirkes and D. Zeppenfeld, *Phys. Lett.* **B 380** (1996) 205;
E. Mirkes, preprint TTP-97-39 (1997), hep-ph/9711224.

[12] S. Catani and M.H. Seymour, *Nucl. Phys.* **B 485** (1997) 291, Erratum-ibid. **B 510** (1997) 503.

[13] D. Graudenz, hep-ph/9710244.

[14] B. Pötter, *Comp. Phys. Commun.* **119** (1999) 45.

[15] C. Duprel et al, Proc. of the Workshop on Monte Carlo Generators for HERA Physics, eds. A. Doyle, G. Grindhammer, G. Ingelman, H. Jung, Hamburg (1999);
B. Pötter, hep-ph/9911221.

[16] CTEQ Collab., H.L Lai et al., *Phys. Rev.* **D 55** (1997) 1280.

[17] G. Ingelman, A. Edin and J. Rathsman, *Comp. Phys. Commun.* **101** (1997) 108.

[18] H. Jung, *Comp. Phys. Commun.* **86** (1995) 147.

[19] L. Lönnblad, *Comp. Phys. Commun.* **71** (1992) 15.

[20] G. Gustafson, *Phys. Lett.* **B 175** (1986) 453;
B. Andersson, G. Gustafson, L. Lönnblad and U. Pettersson, *Z. Phys.* **C 43** (1989) 625;
G. Gustafson and U. Pettersson, *Nucl. Phys.* **B 306** (1988) 746.

[21] L. Lönnblad, *Z. Phys.* **C 65** (1995) 285;
A.H. Mueller, *Nucl. Phys.* **B 415** (1994) 373;
L. Lönnblad, *Z. Phys.* **C 70** (1996) 107.

[22] T. Sjöstrand, *Comp. Phys. Commun.* **39** (1986) 347;
T. Sjöstrand and M. Bengtsson, *Comp. Phys. Commun.* **43** (1987) 367;
T. Sjöstrand, CERN-TH.6488/92 (1992).

[23] H1 Collab., I. Abt et al., *Nucl. Instrum. Methods* **A 386** (1997) 310 and 348.

[24] H1 SPACAL Group, R.D. Appuhn et al., *Nucl. Instrum. Methods* **A 374** (1996) 149;
H1 SPACAL Group, R.D. Appuhn et al., *Nucl. Instrum. Methods* **A 386** (1997) 397.

[25] H1 Calorimeter Group, B. Andrieu et al., *Nucl. Instrum. Methods* **A 336** (1993) 460.

[26] H1 Calorimeter Group, B. Andrieu et al., *Nucl. Instrum. Methods* **A 344** (1994) 492; *Nucl. Instrum. Methods* **A 350** (1994) 57.

[27] H1 Calorimeter Group, B. Andrieu et al., *Nucl. Instrum. Methods* **A 372** (1996) 399.

[28] J. Bürger et al., *Nucl. Instrum. Methods* **A 279** (1989) 217.

[29] S.D. Ellis and D.E. Soper, *Phys. Rev.* **D 48** (1993) 3160;
S. Catani, Yu.L. Dokshitzer, M.H. Seymour and B.R. Webber, *Nucl. Phys.* **B 406** (1993) 187.

[30] H1 Collab., C. Adloff et al., *Nucl. Phys.* **B 545** (1999) 3.

[31] S. Bentveltsen et al., Proc. of the Workshop on Physics at HERA, Vol. 1, eds. W. Buchmüller and G. Ingelman, Hamburg (1991) 23;
K.C. Hoeger, ibid., 43.

[32] H1 Collab., C. Adloff et al., *Phys. Lett.* **B 462** (1999) 440.

[33] A. Kwiatkowski, H. Spiesberger and H.-J. Möhring, *Comp. Phys. Commun.* **69** (1992) 155.

[34] ZEUS Collab., J. Breitweg et al., *Phys. Lett.* **B 474** (2000) 223.

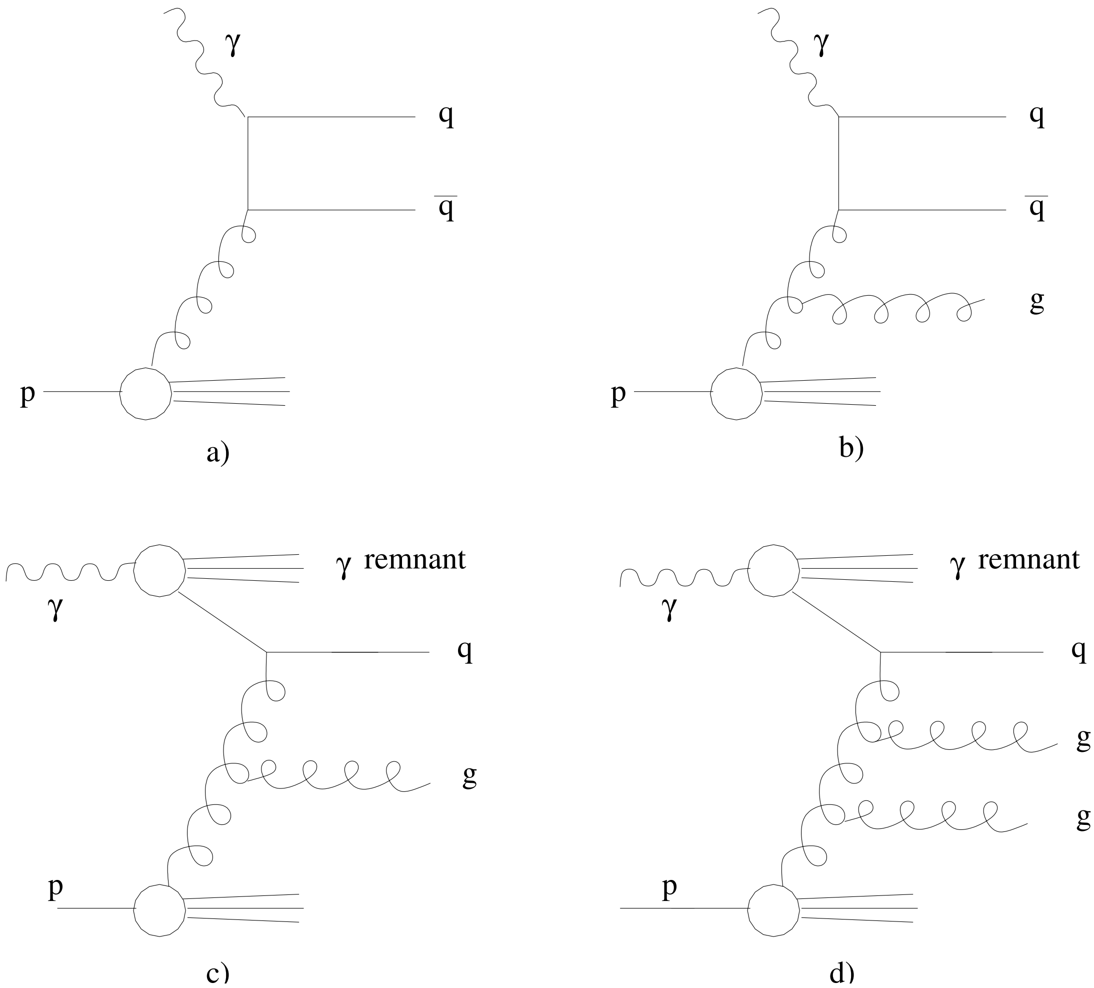

Figure 1: Examples of contributions to the inclusive jet cross section at different orders of the strong coupling constant for direct and resolved photon processes; a: direct process at $\mathcal{O}(\alpha_s)$ (LO); b: direct process at $\mathcal{O}(\alpha_s^2)$ (NLO); c: resolved process at $\mathcal{O}(\alpha_s^2)$ (LO); d: resolved process at $\mathcal{O}(\alpha_s^3)$ (NLO);

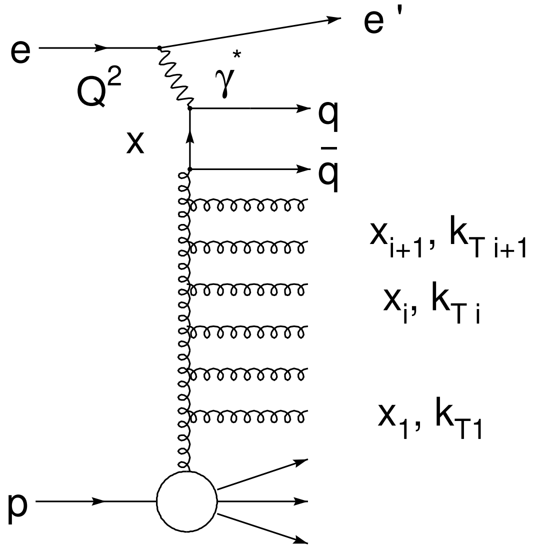

Figure 2: Example of a ladder diagram. Emitted partons are characterised by their transverse momentum k_{Ti}. The longitudinal components of the momenta are labelled x_i.

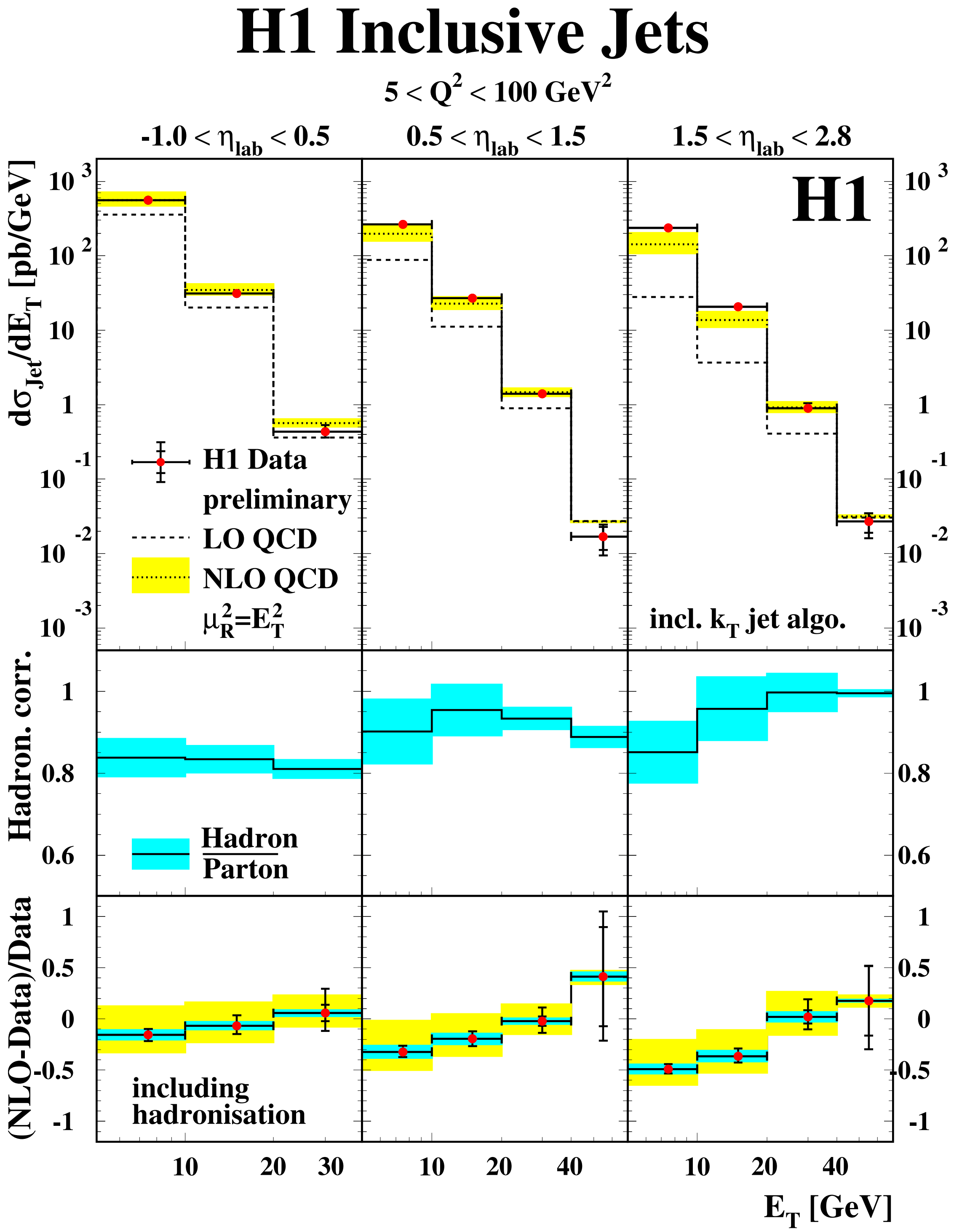

Figure 3: Single-inclusive jet cross section $d\sigma_{Jet}/dE_T$ as a function of E_T in three regions of the pseudorapidity. In the top part the data are compared to LO (dashed line) and NLO QCD predictions (dotted line) obtained with DISENT using $\mu_R^2 = E_T^2$; the shaded band indicates the uncertainty on the NLO QCD prediction obtained by varying the squared renormalization scale by a factor 4 up and down. The center part displays the hadronisation corrections. In the bottom part the expression $(NLO - Data)/Data$ is shown, where NLO means NLO QCD predictions with hadronisation corrections applied.

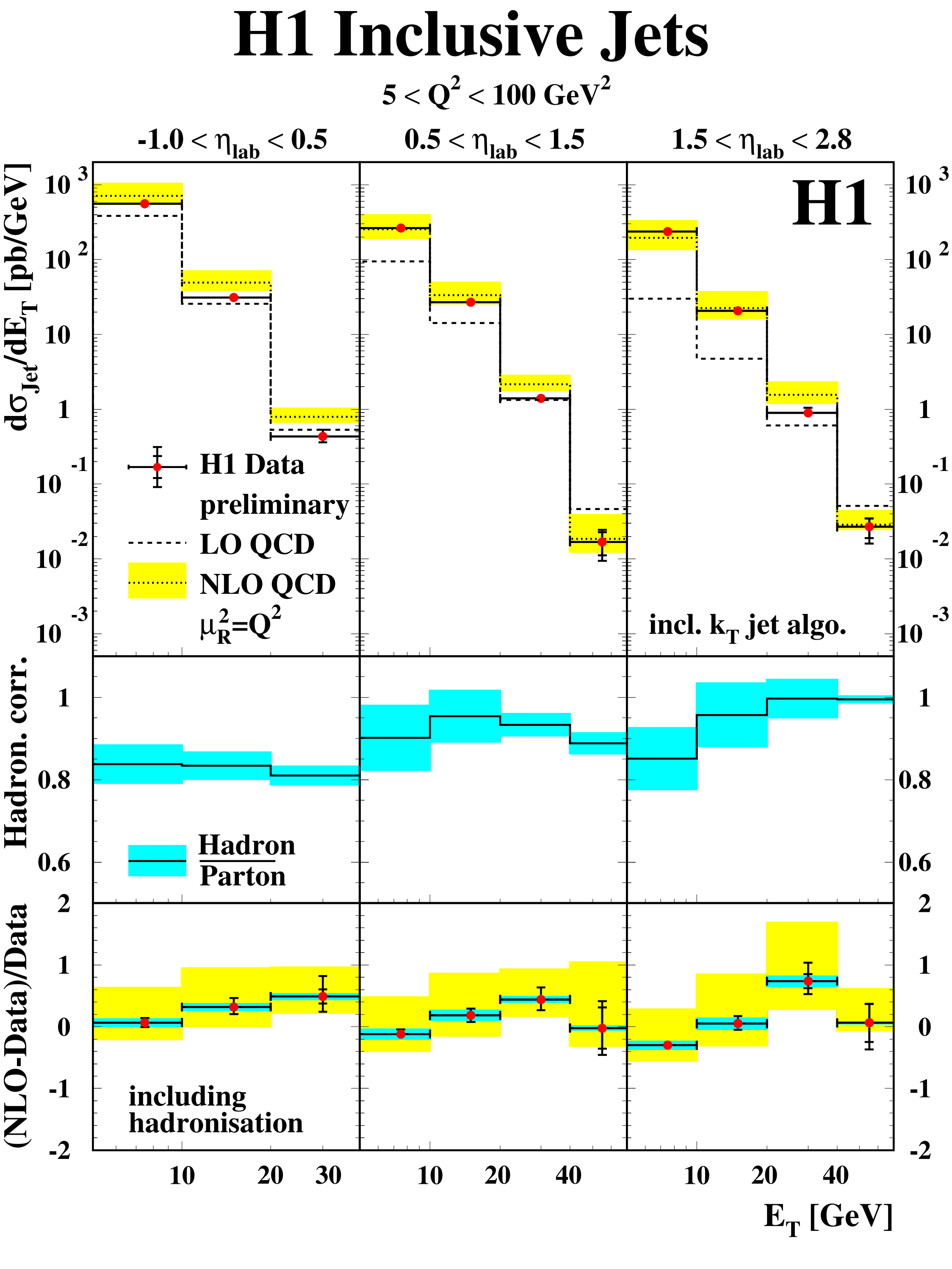

Figure 4: As fig. 3, but for a renormalization scale $\mu_R^2 = Q^2$.

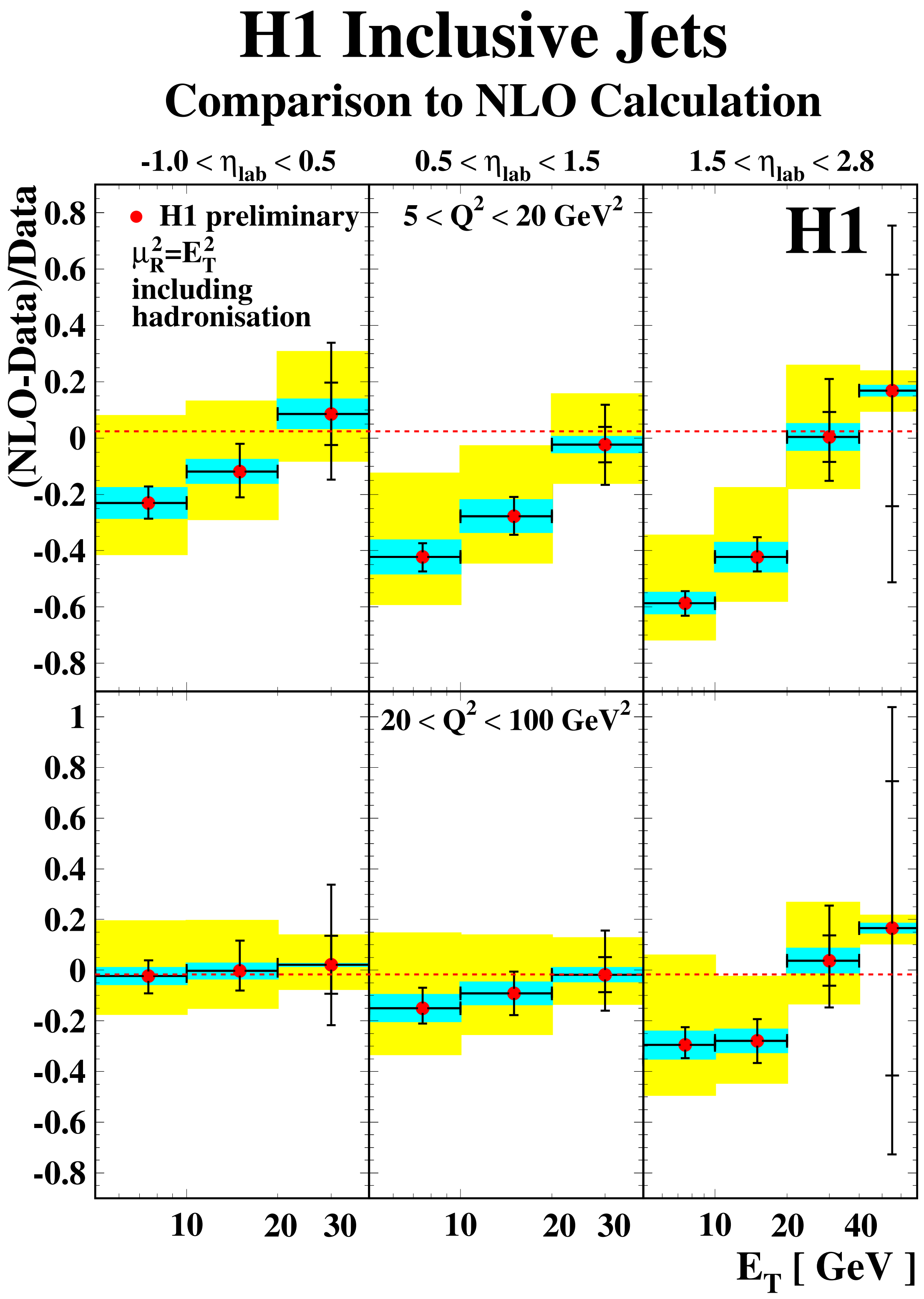

Figure 5: $(NLO - Data)/Data$ for the single-inclusive jet cross section $d\sigma_{Jet}/dE_T$ as a function of E_T in three regions of the pseudorapidity for DISENT predictions using $\mu_R^2 = E_T^2$. Top: $5 < Q^2 < 20\ \mathrm{GeV}^2$, bottom: $20 < Q^2 < 100\ \mathrm{GeV}^2$. NLO includes hadronisation corrections.

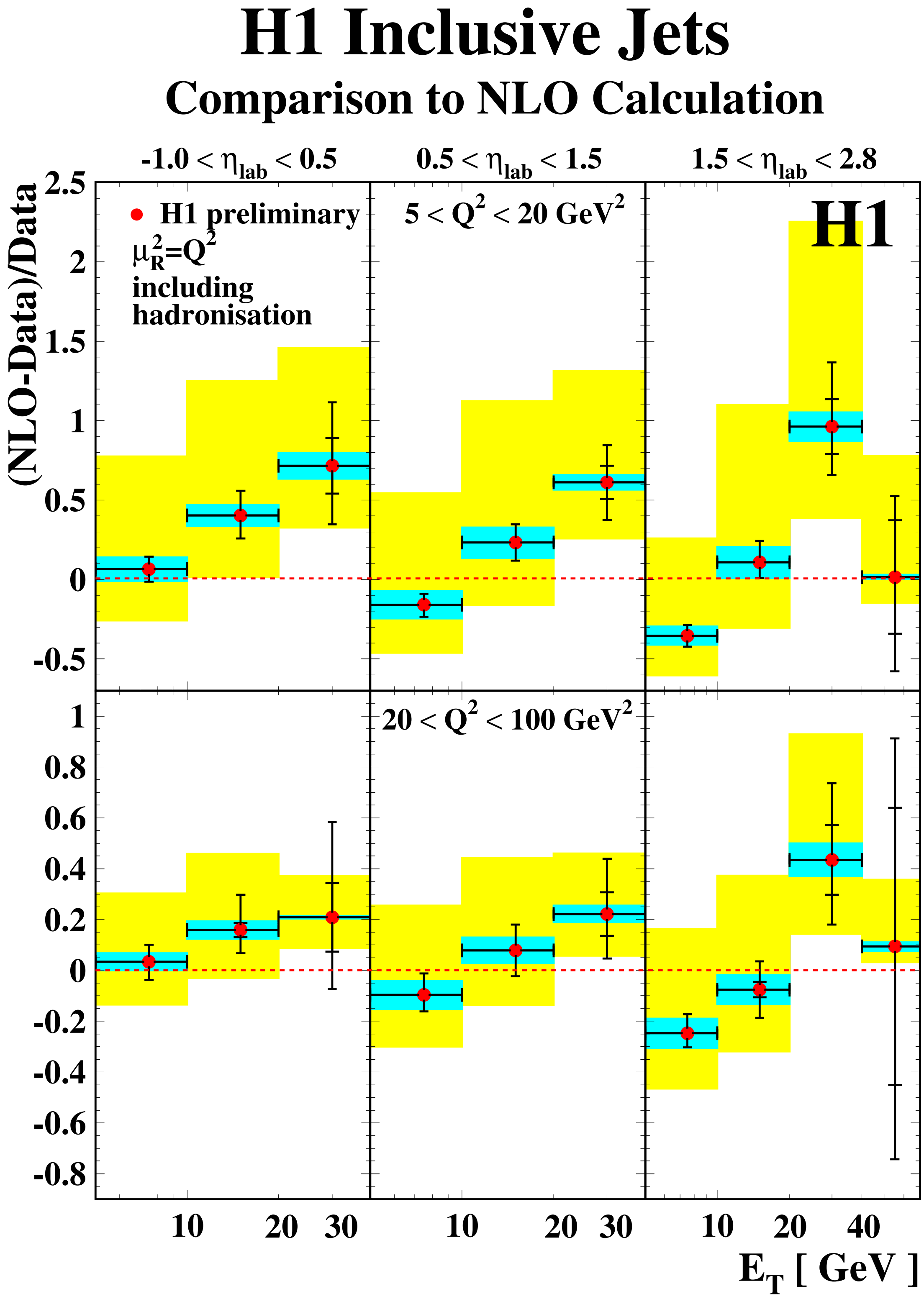

Figure 6: As fig. 5, but for a renormaliation scale $\mu_R^2 = Q^2$.

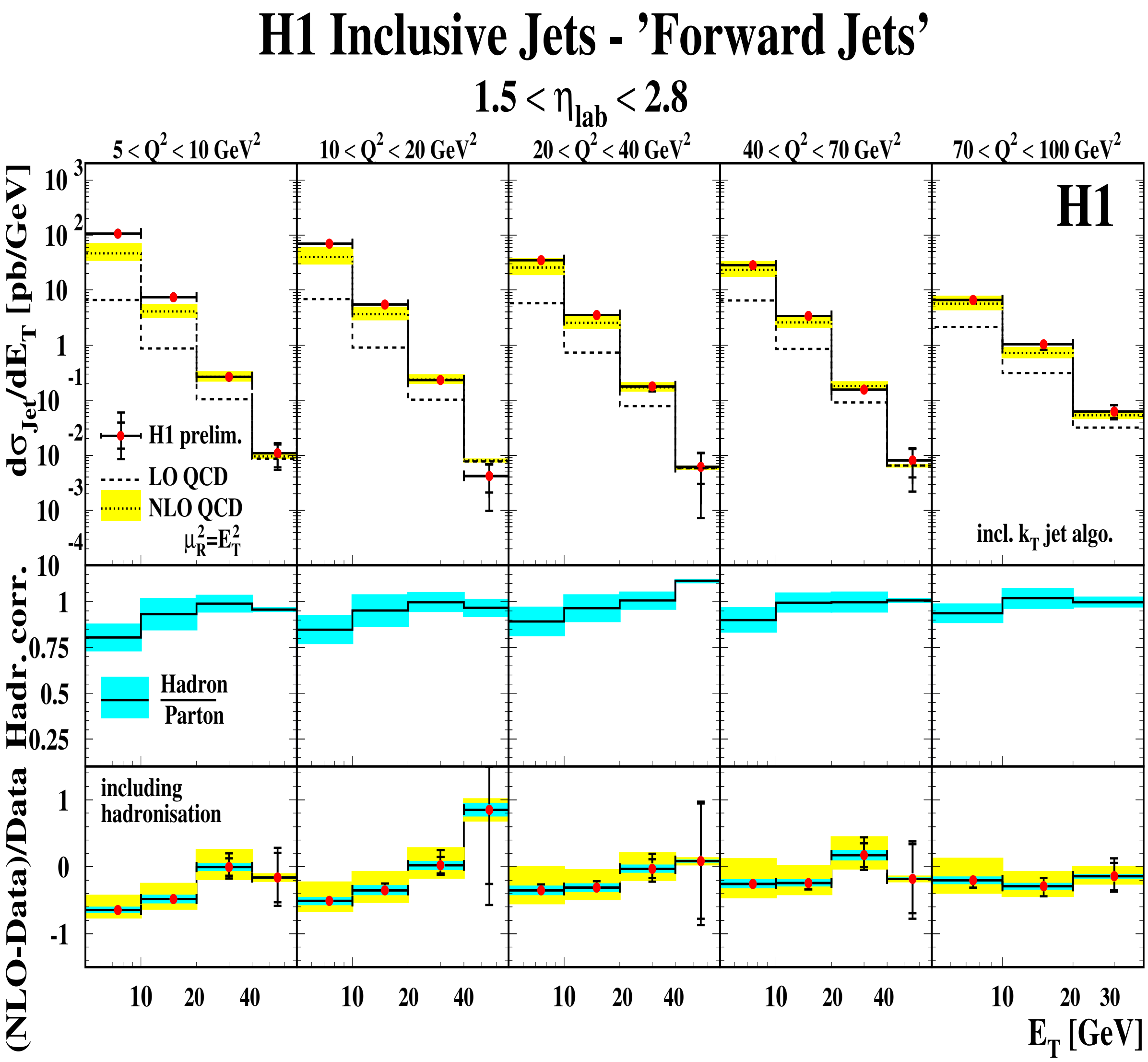

Figure 7: Single-inclusive jet cross section $d\sigma_{Jet}/dE_T$ as a function of E_T in five ranges of the photon virtuality for the forward detector region. In the top part the data are compared to LO (dashed line) and NLO QCD predictions (dotted line) obtained with DISENT using $\mu_R^2 = E_T^2$; the shaded band indicates the uncertainty on the NLO QCD prediction obtained by varying the squared renormalization scale by a factor 4 up and down. The center part displays the hadronisation corrections. In the bottom part the expression $(NLO - Data)/Data$ is shown, where NLO means NLO QCD predictions with hadronisation corrections applied.

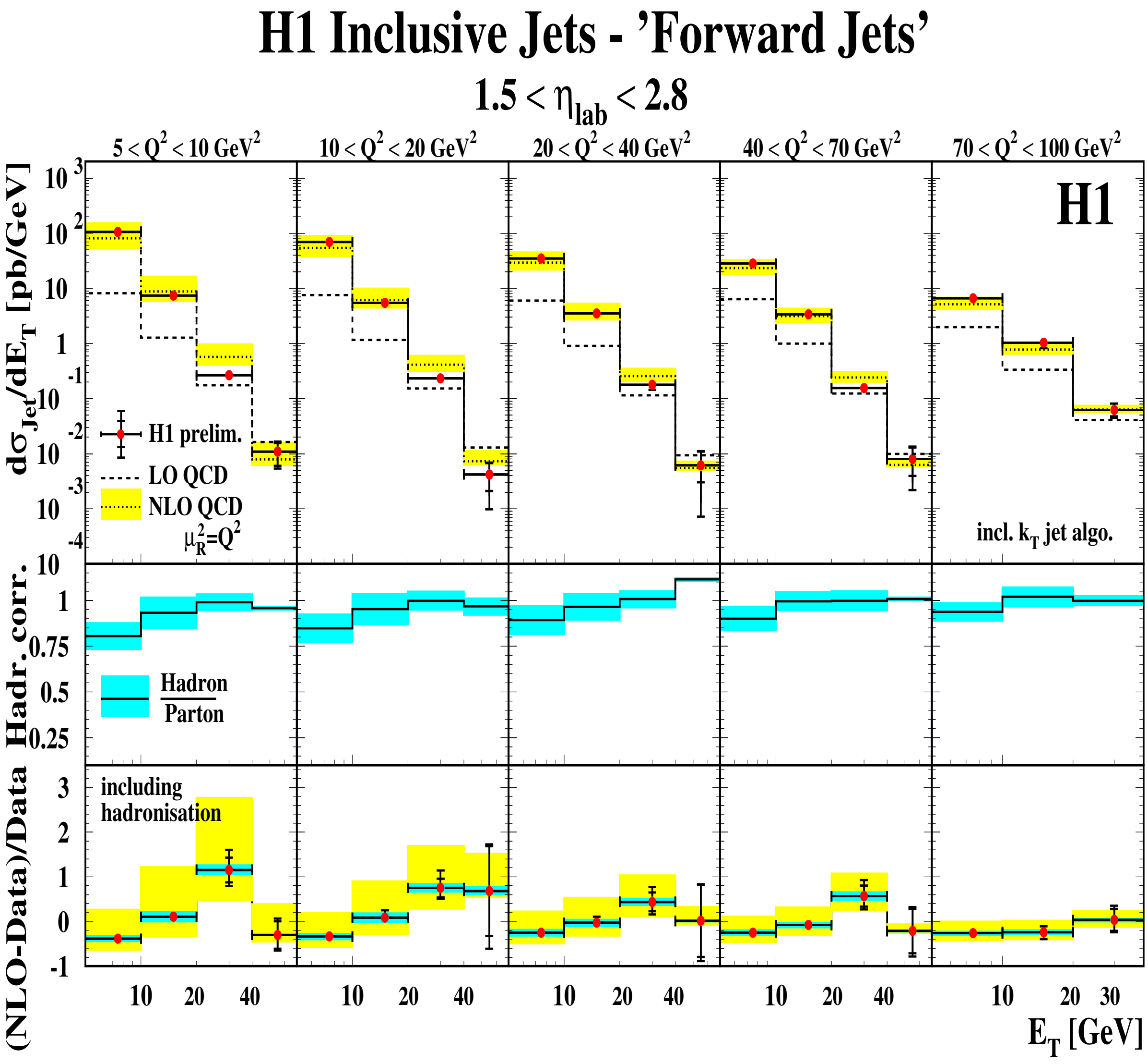

Figure 8: As fig. 7, but for a renormaliation scale $\mu_R^2 = Q^2$.

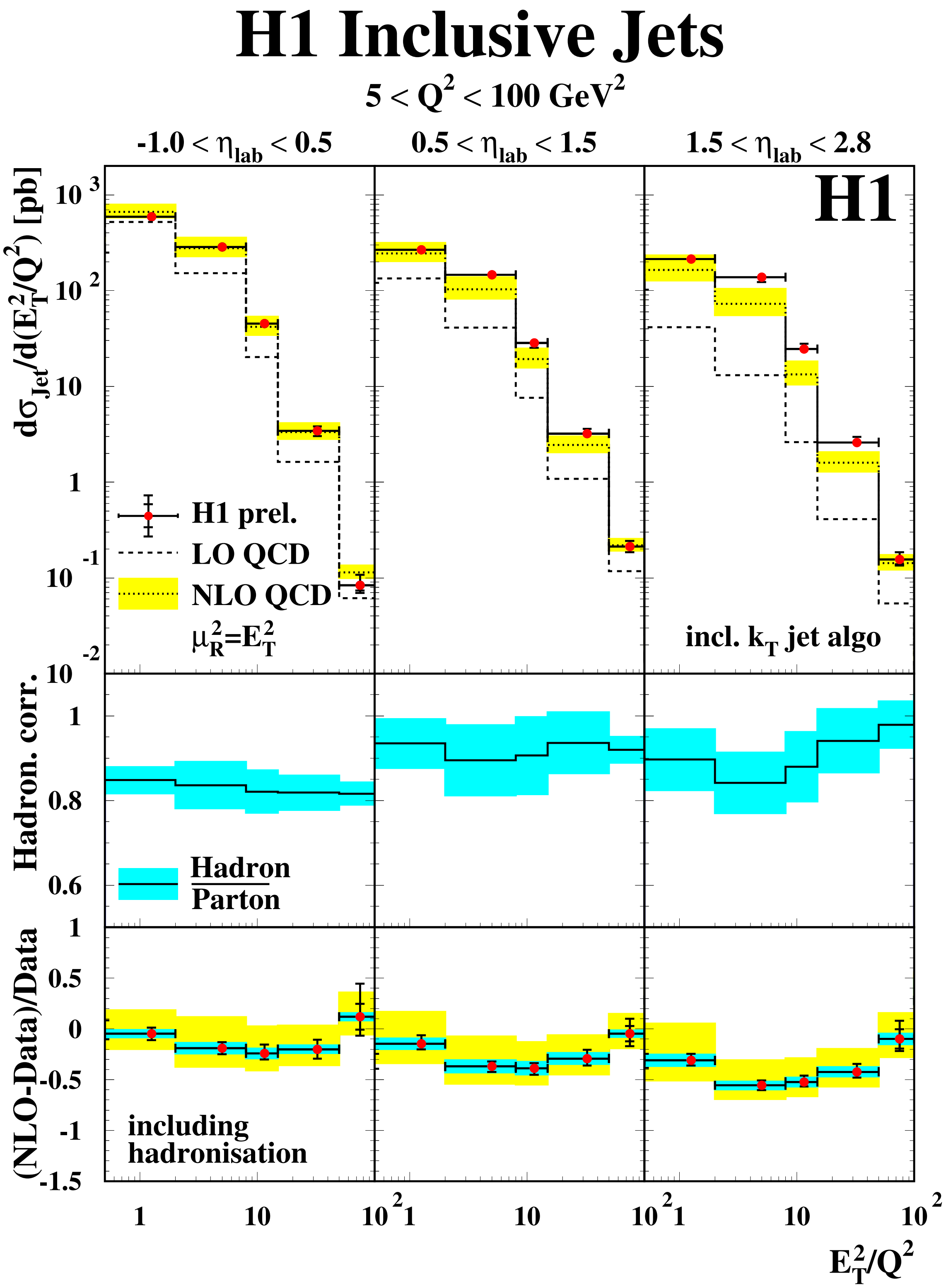

Figure 9: Single-inclusive jet cross section $d\sigma_{Jet}/d(E_T^2/Q^2)$ as a function of E_T^2/Q^2 in three regions of the pseudorapidity. In the top part the data are compared to LO (dashed line) and NLO QCD predictions (dotted line) obtained with DISENT using $\mu_R^2 = E_T^2$; the shaded band indicates the uncertainty on the NLO QCD prediction obtained by varying the squared renormalization scale by a factor 4 up and down. The center part displays the hadronisation corrections. In the bottom part the expression $(NLO - Data)/Data$ is shown, where NLO means NLO QCD predictions with hadronisation corrections applied.

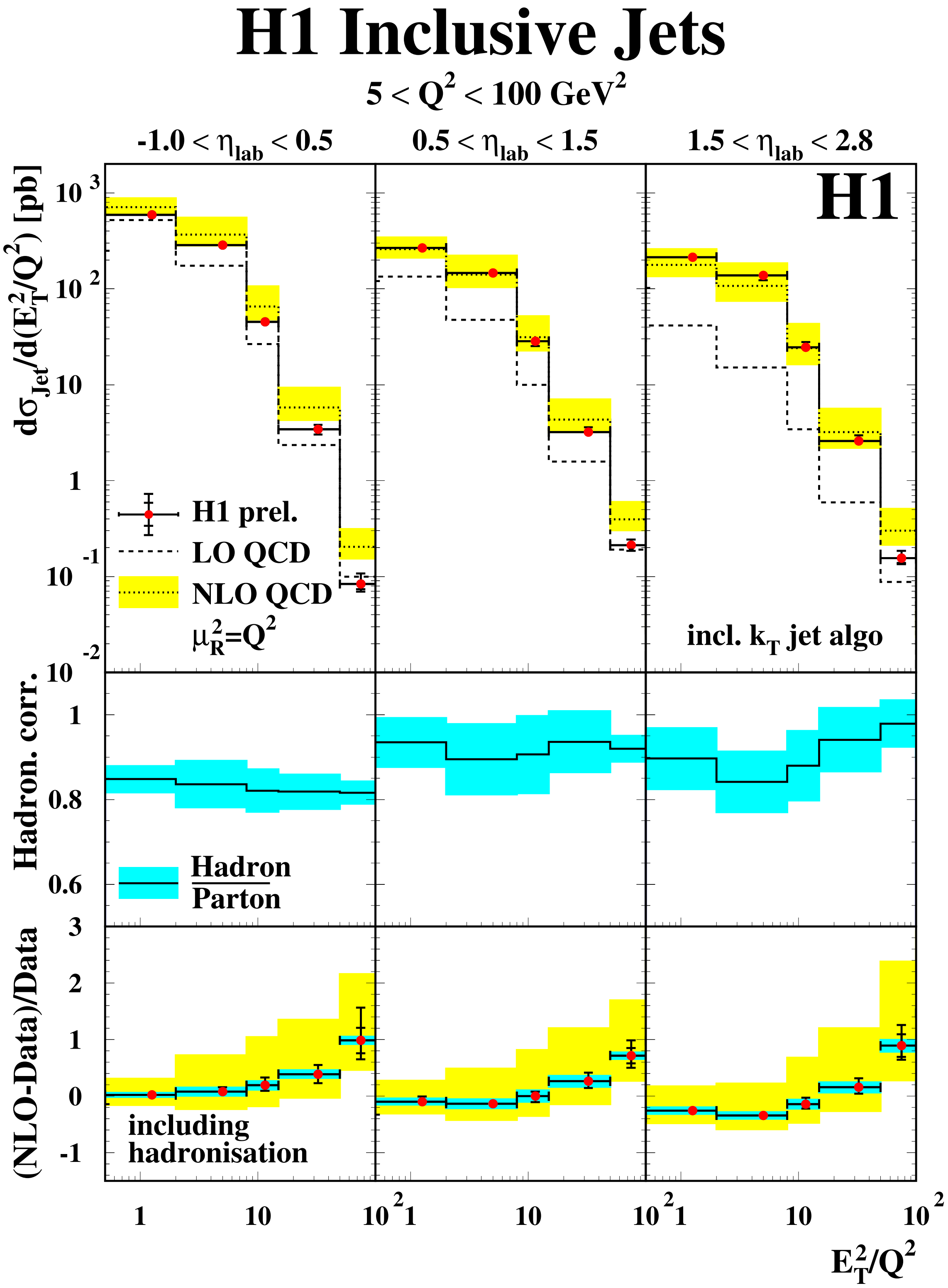

Figure 10: As fig. 9, but for a renormalization scale $\mu_R^2 = Q^2$.

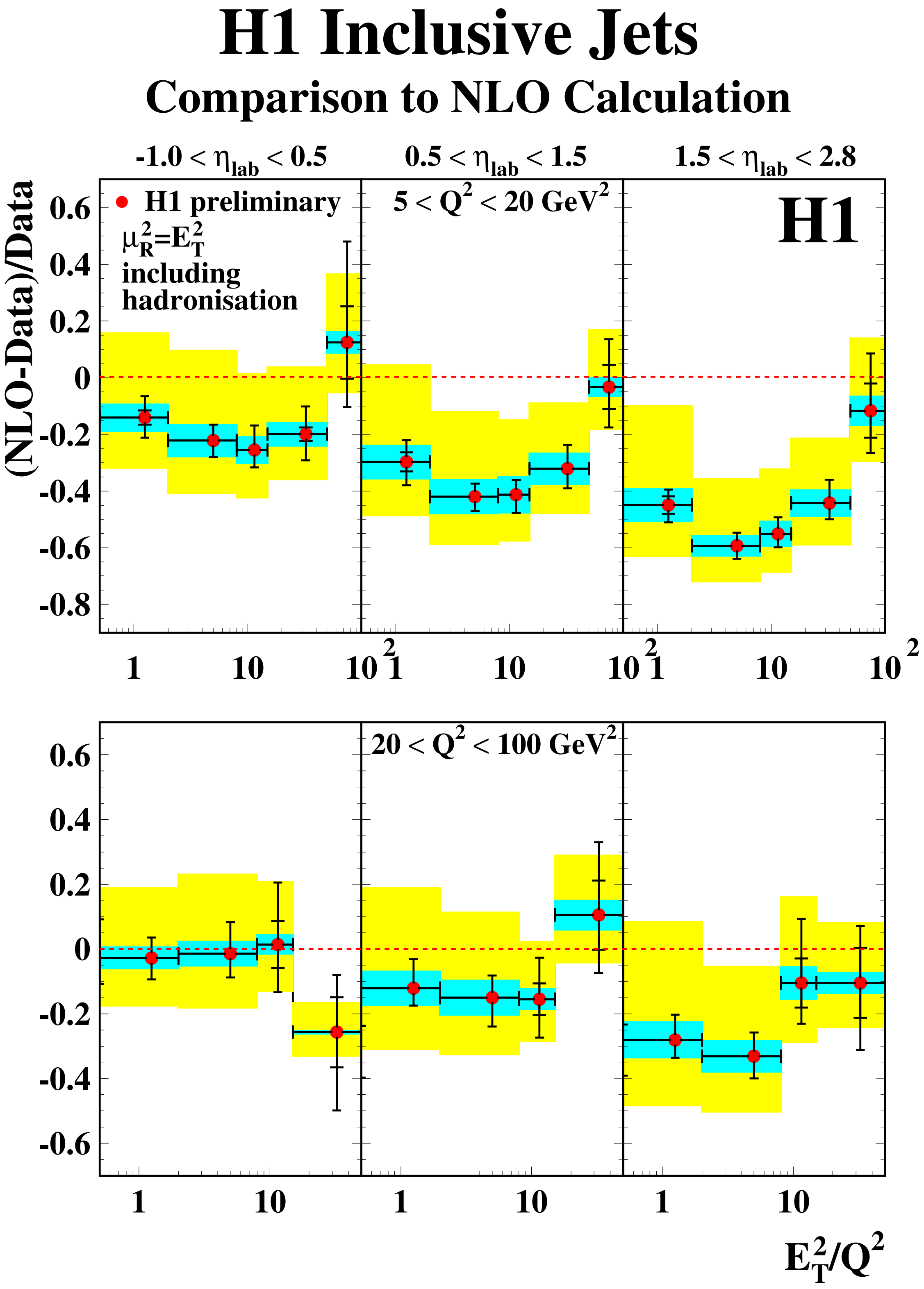

Figure 11: $(NLO - Data)/Data$ for the single-inclusive jet cross section $d\sigma_{Jet}/d(E_T^2/Q^2)$ as a function of E_T^2/Q^2 in three regions of the pseudorapidity for DISENT predictions using $\mu_R^2 = E_T^2$. Top: $5 < Q^2 < 20\ \mathrm{GeV}^2$, bottom: $20 < Q^2 < 100\ \mathrm{GeV}^2$. NLO includes hadronisation corrections.

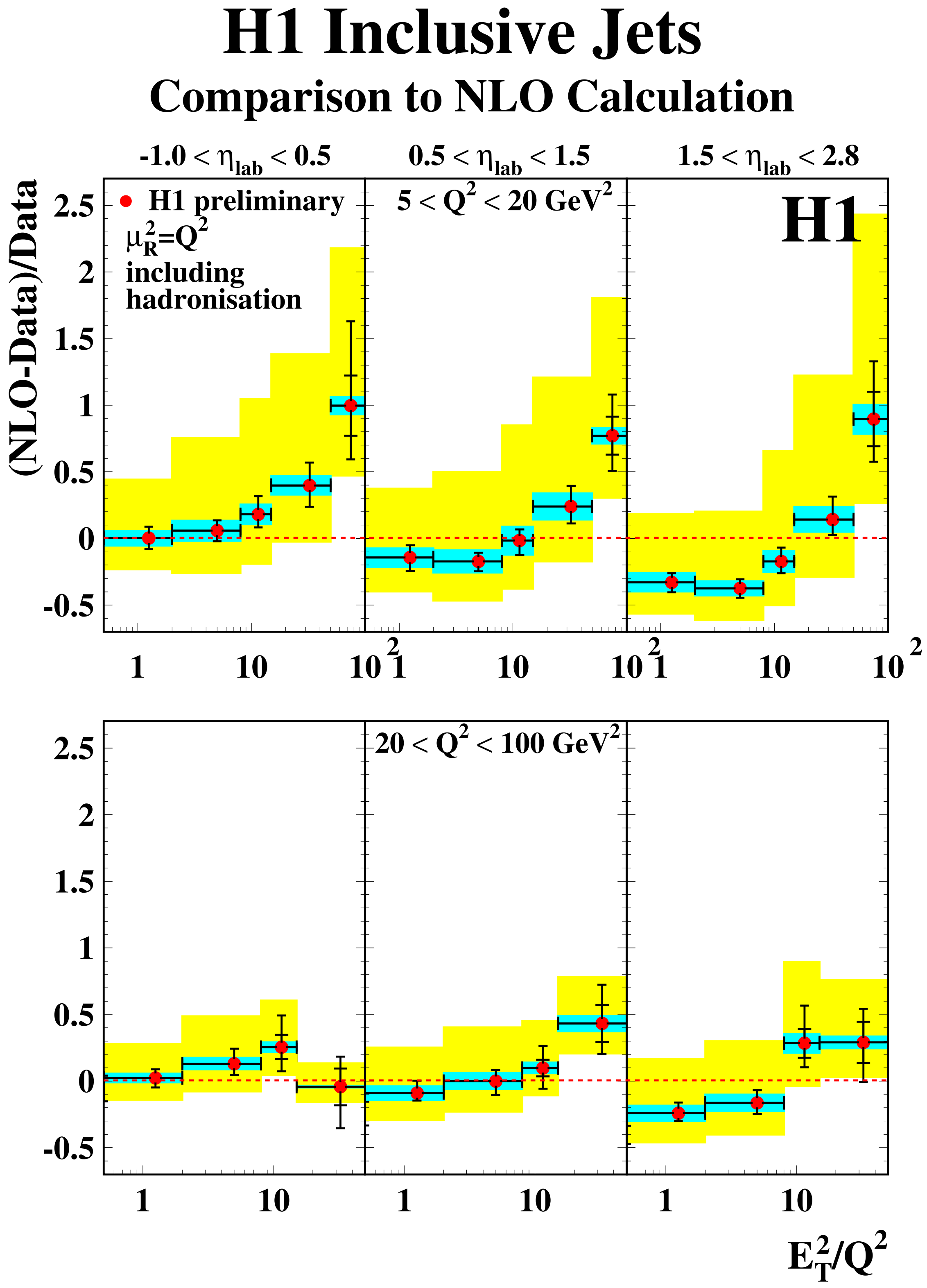

Figure 12: As fig. 11, but for a renormalization scale $\mu_R^2 = Q^2$.

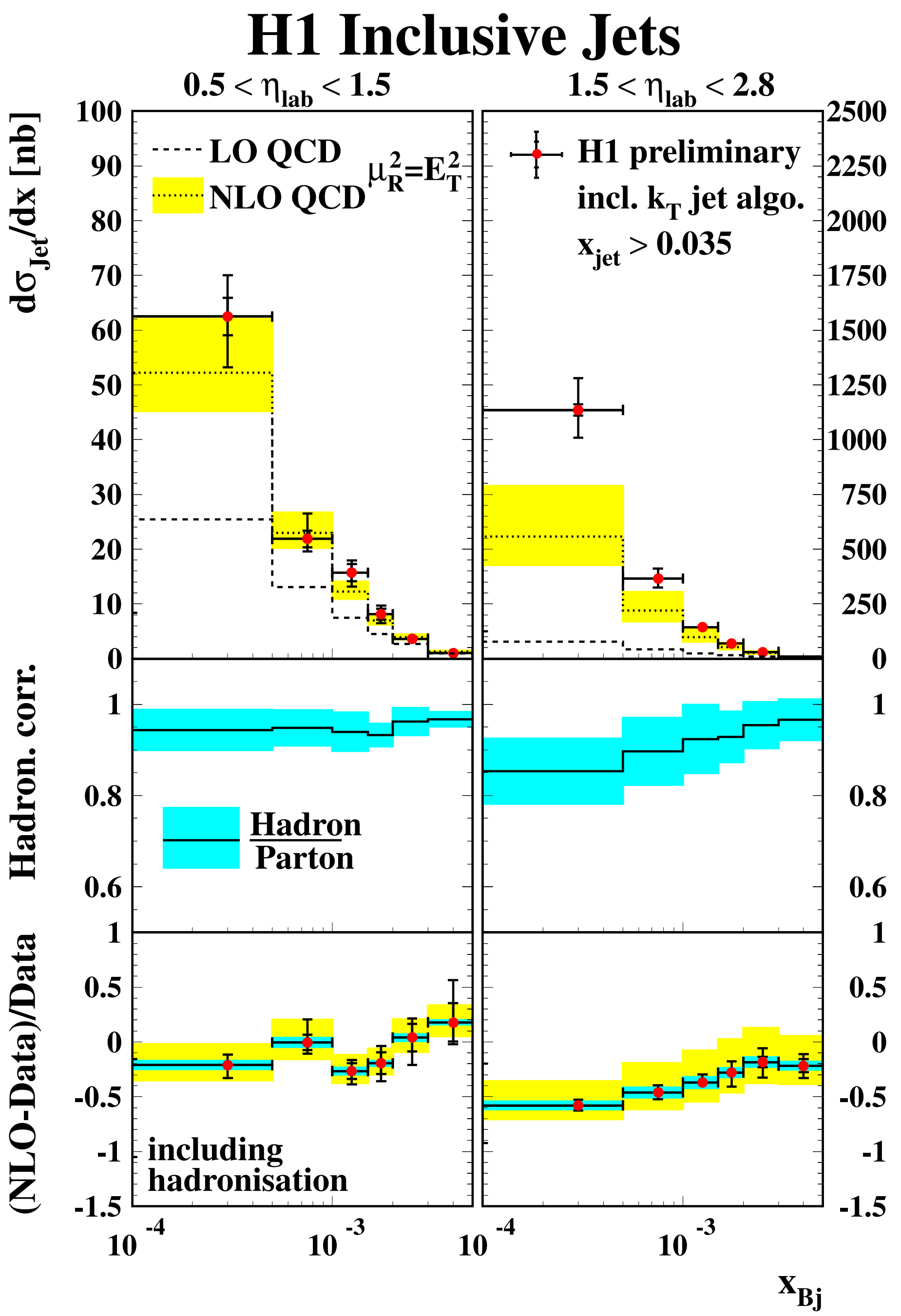

Figure 13: Single-inclusive jet cross section $d\sigma_{Jet}/dx_{Bj}$ as a function of x_{Bj} in two regions of the pseudorapidity for $5 < Q^2 < 100\ \mathrm{GeV}^2$. In the top part the data are compared to LO (dashed line) and NLO QCD predictions (dotted line) obtained with DISENT using $\mu_R^2 = E_T^2$; the shaded band indicates the uncertainty on the NLO QCD prediction obtained by varying the squared renormalization scale by a factor 4 up and down. The center part displays the hadronisation corrections. In the bottom part the expression $(NLO - Data)/Data$ is shown, where NLO means NLO QCD predictions with hadronisation corrections applied.

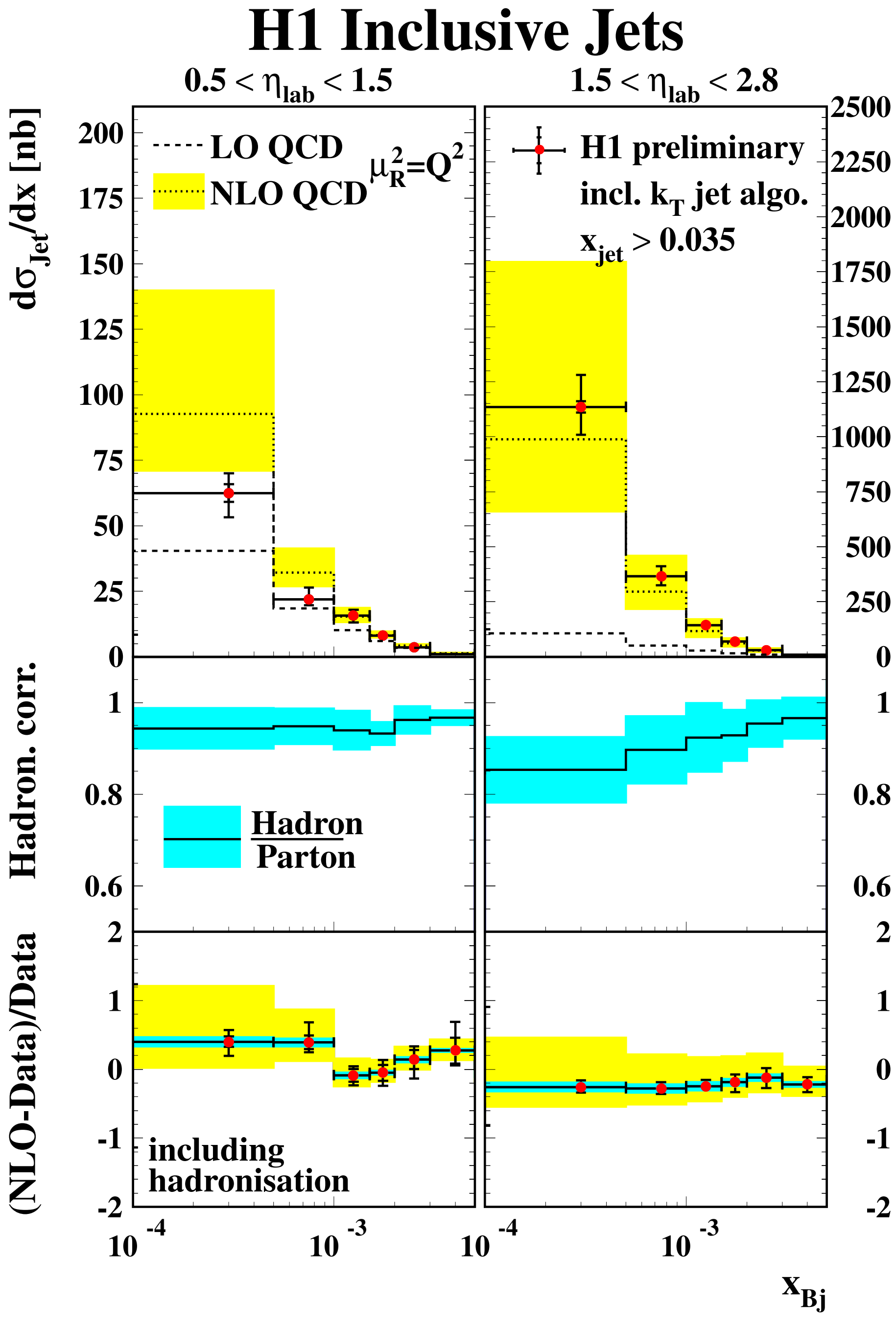

Figure 14: As fig. 13, but for a renormalization scale $\mu_R^2 = Q^2$.

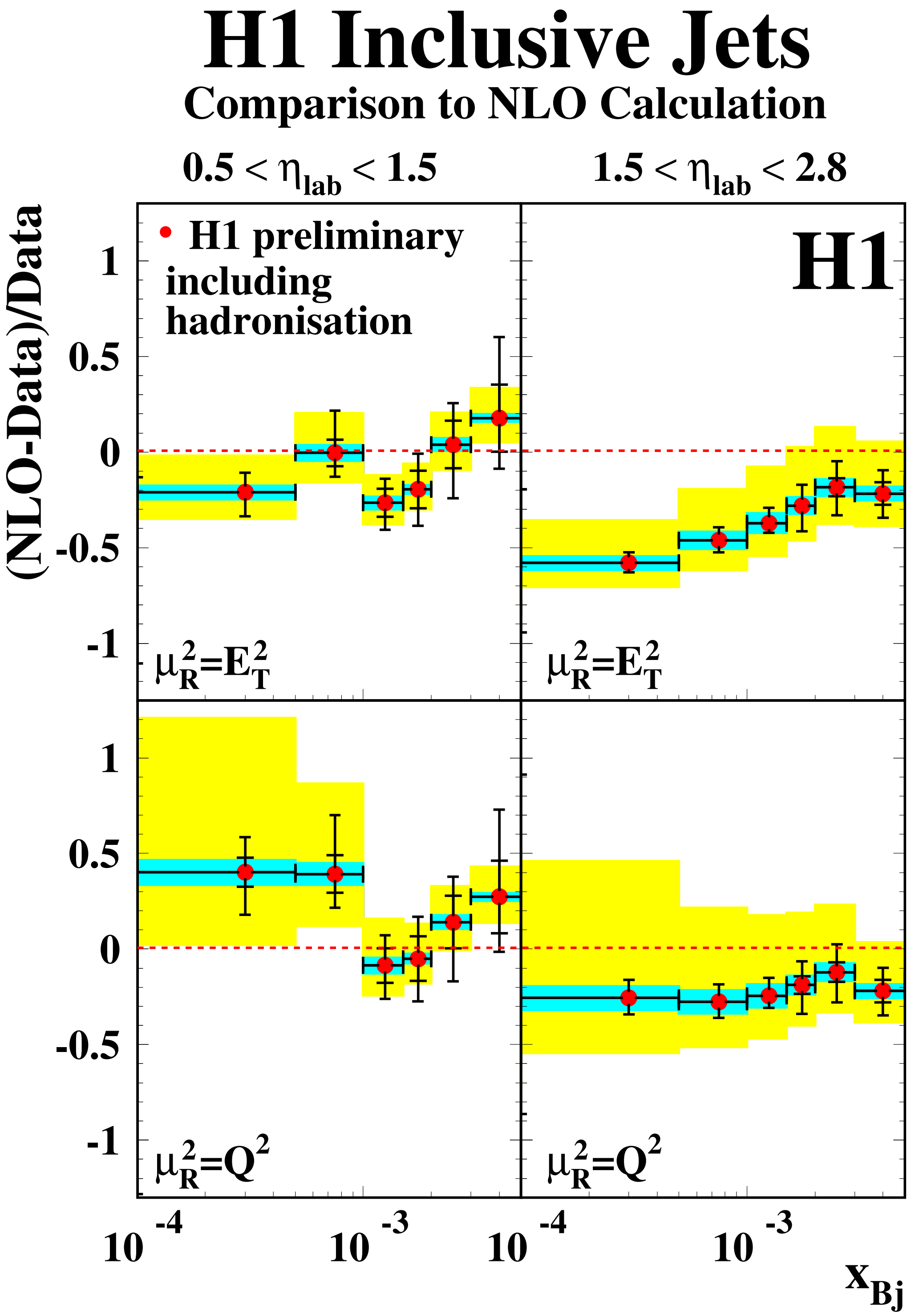

Figure 15: $(NLO - Data)/Data$ for the single-inclusive jet cross section $d\sigma_{Jet}/dx_{Bj}$ as a function of x_{Bj} in two regions of the pseudorapidity for the DISENT predictions and for for $5 < Q^2 < 100$ GeV^2. Top: $\mu_R^2 = E_T^2$, bottom: $\mu_R^2 = Q^2$. NLO includes hadronisation corrections.

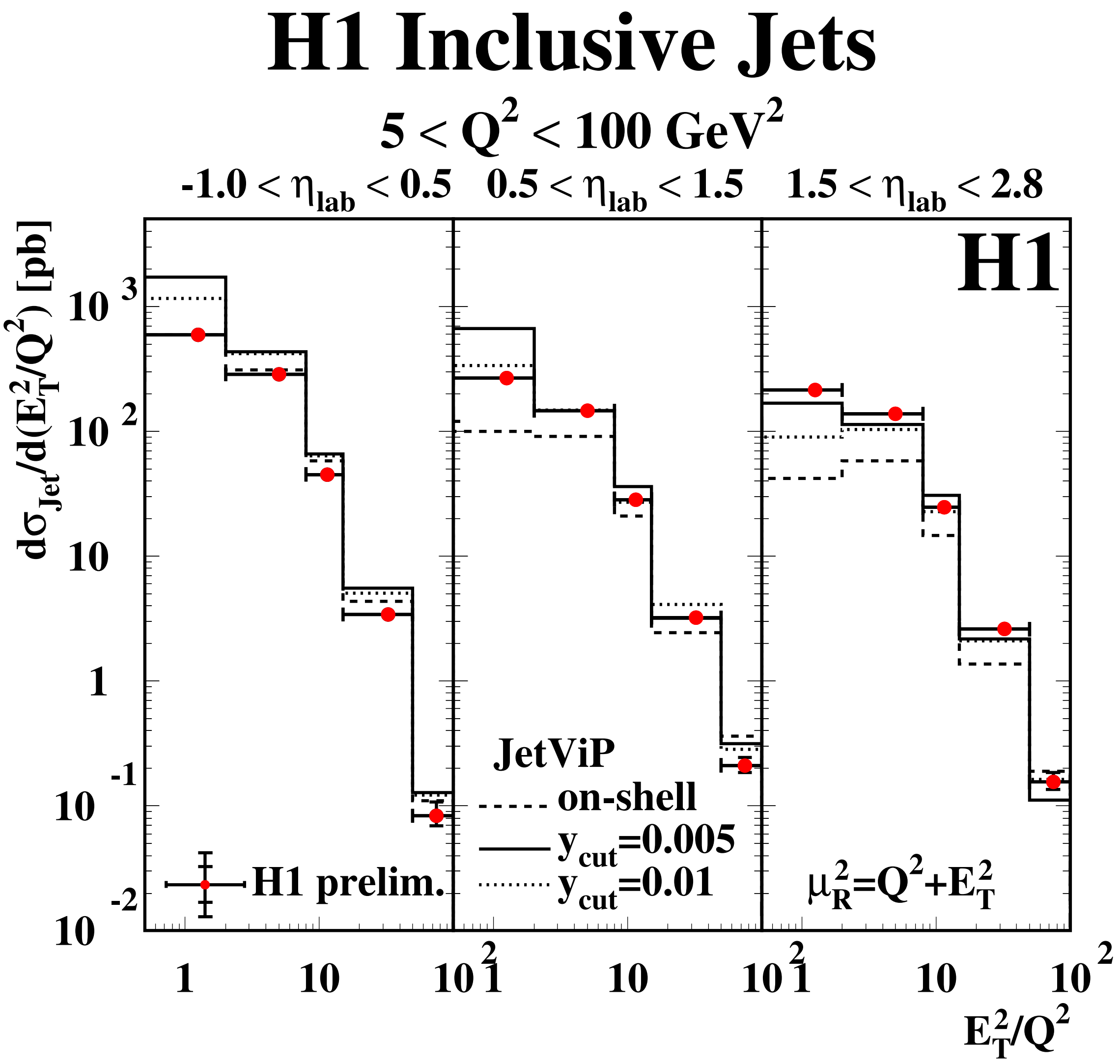

Figure 16: Single-inclusive jet cross section $d\sigma_{Jet}/d(E_T^2/Q^2)$ as a function of E_T^2/Q^2 in three regions of the pseudorapidity. The data points are compared to three different JetViP calculations. The two scenarios labelled $y_{cut} = 0.005$ and $y_{cut} = 0.01$ correspond to the off-shell scheme. For the on-shell scheme there is no dependence on the y_{cut} parameter.